



Cite this: *Phys. Chem. Chem. Phys.*,
2020, 22, 17668

Probing the structural and electronic response of Magnus green salt compounds $[\text{Pt}(\text{NH}_2\text{R})_4][\text{PtCl}_4]$ ($\text{R} = \text{H}, \text{CH}_3$) to pressure†

Jonathan G. Richardson,^a Helen Benjamin,^a Stephen A. Moggach,^{id} ^{*b}
Lisette R. Warren,^{id} ^a Mark R. Warren,^c David R. Allan,^{id} ^c Lucy K. Saunders,^{id} ^c
Carole A. Morrison^{*a} and Neil Robertson^{id} ^{*a}

Despite possessing the desirable crystal packing and short Pt...Pt stacking distances required for a large piezoresistive response, the conductivity-pressure response of the Magnus green salt $[\text{Pt}(\text{NH}_3)_4][\text{PtCl}_4]$ is extremely sluggish. Through a combination of high-pressure X-ray diffraction and hybrid-DFT solid state calculations this study demonstrates that the poor conductivity-pressure response is due to a low volumetric compression anisotropy, a relatively large ambient pressure band gap and a lack of dispersion in the conduction band. Ligand modification (from NH_3 to NH_2CH_3) does not enhance the piezoresistive response, causing even lower anisotropy of the volumetric compression and an unexpected phase transition at above 2 GPa. This study demonstrates that consideration of frontier band dispersion is a key design criterion, alongside crystal packing and Pt...Pt stacking distances, for piezoresistive materials.

Received 18th June 2020,
Accepted 24th July 2020

DOI: 10.1039/d0cp03280h

rsc.li/pccp

Introduction

Since the discovery of the first organic semiconductors in 1954 there has been considerable research into the electrical properties of molecular-based materials,¹ leading to the discovery of exotic behaviours such as superconductivity,² Dirac electron systems,³ and Mott-insulators.⁴ One class of materials that are of particular interest are single-component molecular metals; neutral molecules that exhibit metallic conductive behaviour. Several examples have been reported based on transition metal dithiolene complexes,⁵ particularly complexes of Au,^{6–12} Ni,^{7,12,13} and Pd.¹⁴ Conductivity in these systems arises when strong intermolecular interactions give rise to a narrow band gap and favourable orbital overlaps.⁵ In systems where the band gap is larger, application of external pressure can be used to induce a transition to a metallic state by increasing the intermolecular interactions. This behaviour has been reported for gold¹⁵ and nickel¹⁶ dithiolene complexes, and also for a

series of platinum complexes with 1,2-dionedioximato ligands that form one-dimensional stacks in the solid state.^{17–22}

Our recent work,²³ via the combination of high-pressure X-ray diffraction and hybrid density functional theory (DFT), interpreted the piezoresistive behaviour of platinum bis(1,2-benzoquinonedioximato), hereafter $\text{Pt}(\text{bqd})_2$,²⁴ and platinum bis(1,2-dimethylglyoximato), hereafter $\text{Pt}(\text{dmg})_2$,²⁵ two members of the aforementioned group of platinum 1,2-dionedioximato complexes. Whilst the metal...metal stacking provides a conductive pathway, both the stacking distance and the steric and electronic nature of the ligand contribute towards the conductivity behaviour at ambient and non-ambient conditions, indicating that the piezoresistive effect can be tuned by both crystal packing and molecular design.

Following on from our earlier study, we now extend our investigation to other platinum species containing short (< 3.50 Å) metal...metal stacking distances, namely two Magnus green salts $[\text{Pt}(\text{NH}_2\text{R})_4][\text{PtCl}_4]$, where $\text{R} = \text{H}$ (hereafter MagNH_3) and $\text{R} = \text{CH}_3$ (hereafter MagNH_2Me). Piezoresistive behaviour has previously been reported for MagNH_3 ,²⁶ and MagNH_2Me was chosen to determine the effect of a modest ligand modification on the material response to pressure.

MagNH_3 crystallises in the $P4/mnc$ space group ($a = 9.98$ Å, $c = 6.46$ Å) and consists of 1-D chains of alternating platinum(II)tetraammine and tetrachloroplatinate(II) units along the crystallographic c -axis (Fig. 1A).²⁷ The intra-chain Pt...Pt distance (3.23 Å) equates to half the value of the c -axis lattice parameter. Within the 1-D chains, NH_3 and Cl groups on

^a EaStCHEM School of Chemistry, University of Edinburgh, Edinburgh, UK.
E-mail: neil.robertson@ed.ac.uk

^b Centre for Microscopy, Characterisation and Analysis, University of Western Australia, 35 Stirling Highway, Crawley, Perth, 6005, Western Australia, Australia

^c Diamond Light Source, Diamond House, Harwell Science & Innovation Campus, Didcot, Oxfordshire, OX11 0DE, UK

† Electronic supplementary information (ESI) available: Crystallographic information, visualisation of crystalline orbitals and band structures for additional pressure points. CCDC 2009951–2009968. For ESI and crystallographic data in CIF or other electronic format see DOI: 10.1039/d0cp03280h



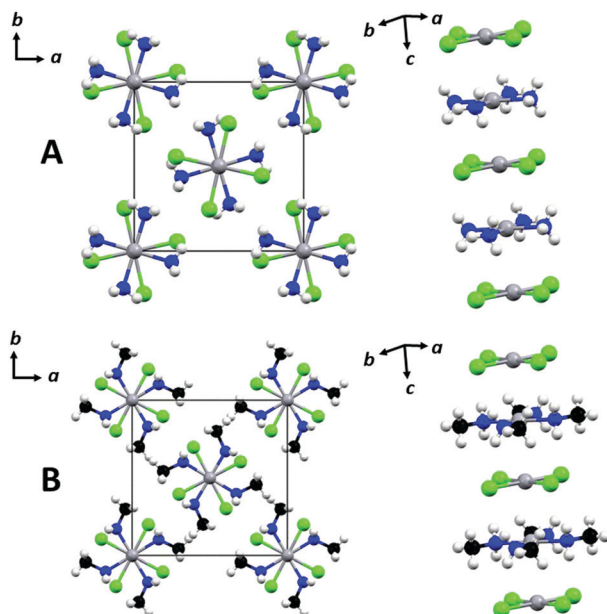


Fig. 1 Crystal packing structures of MagNH_3 (A) and MagNH_2Me (B), indicating the relationship between neighbouring salt units viewed along the [001] (left) and approximately perpendicular to the [001] (right). Atoms are coloured: Pt, dark grey; Cl, green; N, blue; C, black; H, light grey. Unit cell edges are coloured black.

neighbouring $[\text{Pt}(\text{NH}_3)_4]^{2+}$ and $[\text{PtCl}_4]^{2-}$ units are not eclipsed but rather related by a dihedral angle ($\angle \text{Cl-Pt}2 \cdots \text{Pt}1\text{-N}$) of *ca.* -28° . Furthermore, there is an alternation of units between neighbouring chains which are related by a glide plane that runs perpendicular to the [100] direction, and equivalent chains are related by the 4-fold rotation about the *c*-axis direction. This packing arrangement promotes close intra- and inter-chain N-H \cdots Cl distances (2.5–3.0 Å), which have been previously attributed to providing rigidity to the solid state structure.^{27,28}

MagNH_2Me crystallises in the same space group and packing motif as MagNH_3 (Fig. 1B), with increased *a* and *b* unit cell parameters to accommodate the larger ligand (*a* = 10.35 Å, *c* = 6.50 Å).²⁹ Other than a slightly larger intra-chain dihedral angle of *ca.* 31° for MagNH_2Me , which is thus in the opposite direction to that seen in MagNH_3 , the structural differences between the ambient pressure structures of the two complexes are minimal.

Previous high-pressure studies on MagNH_3 showed that the Pt \cdots Pt contact distance decreased by *ca.* 0.12 Å and 0.27 Å at 2 GPa and 10 GPa respectively, indicating a 3.7% and 8.4% contraction compared to the ambient pressure structure,²⁶ and maximum conductivity in compressed pellets occurs at around 10 GPa, with a two-order magnitude change in conductivity over the 0–10 GPa pressure range.⁷ Partial electronic band structure calculations based on compression of a 1D column model have reported a reduction in the band gap from *ca.* 1.0 eV to *ca.* 0.3 eV in response to an inter-column compression of 6%,³⁰ which is comparable to the structural response observed at 3.5 GPa for the full crystal.²⁶

The family of platinum complexes with 1,2-dionedioximate ligands has been shown to exhibit much faster structural responses

to pressure than for MagNH_3 .^{19,21,22} $\text{Pt}(\text{bqd})_2$, in particular, exhibits *ca.* 7% contraction by 2 GPa,^{20,22,23} achieving metallic behaviour by modest pressures of only *ca.* 1 GPa.^{18,20,31,32} The difference in the structure–property relationships of MagNH_3 and $\text{Pt}(\text{bqd})_2$ are surprising given the similarity in crystal packing and ambient-pressure Pt \cdots Pt distances (3.23 Å and 3.17 Å, respectively),²⁴ and points towards the ligand playing an active role in controlling the size of the electronic band gap. In this work we now look to add deeper insight into the existing literature reports on MagNH_3 and MagNH_2Me to obtain full structural characterisation and complete electronic band structure diagrams, and quantify how they change with pressure. The information gained from this study, presented alongside results from our previous study on $\text{Pt}(\text{bqd})_2$ as a comparison,²³ greatly adds to the collective understanding of the intermolecular interactions and electronic properties that result in piezoresistive behaviour in metal complexes.

Results and discussion

X-ray crystallography

Diffraction data were collected to 4.62 GPa and 2.32 GPa for MagNH_3 and MagNH_2Me respectively, with structures refined to 4.62 GPa and 1.92 GPa. In the case of MagNH_3 , the sample remained in the *P4/mnc* space group up to the highest pressure point (Table S1, ESI†). The pressure series was stopped at 4.62 GPa due to well-exceeding the hydrostatic limit of the pressure-transmitting medium,³³ despite no obvious drop in quality of the diffraction data. MagNH_2Me , on the other hand, remained in the *P4/mnc* space group only up to 1.92 GPa (Table S2, ESI†). The unit cell pressure response for MagNH_3 (0–4.62 GPa) and MagNH_2Me (0–1.92 GPa) is given in Fig. 2.

An examination of the unit cell volume across the entire pressure series showed that both compounds compress at a similar rate, achieving around 8% volumetric compression by 2 GPa, and increasing to 14% contraction by 4.62 GPa for

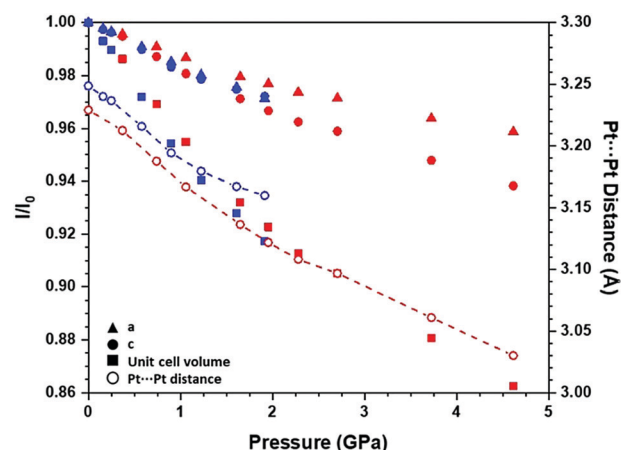


Fig. 2 Pressure response of unit cell parameters of MagNH_3 (red) and MagNH_2Me (blue) (prior to the phase transition) as a fraction of the unit cell parameters obtained at ambient conditions (left ordinate) and consequential decrease of Pt \cdots Pt distance (right ordinate).



MgNH₃. In both cases, this extent of compression was significantly less than that observed for Pt(bqd)₂,^{20,22,23} which achieved 12% volumetric compression by 2 GPa. The higher bulk modulus values for MgNH₃ (18.9(7) GPa) and MgNH₂Me (16.5(9) GPa), obtained by fitting the volumetric compression data to a 3rd order Birch–Murnaghan equation of state (Fig. S1, ESI†),³⁴ highlights the lower rate of compressibility compared to Pt(bqd)₂ (11.7(7) GPa).²³ The similar bulk modulus values for MgNH₃ and MgNH₂Me hide the difference in the contributions to their volumetric compression; an almost even contribution from the *a* and *c* axes was observed for MgNH₂Me, whereas the compression for MgNH₃ was more anisotropic, with a majority contribution from the *c*-axis, and thus the Pt··Pt stacking direction.

From a structural perspective, no significant variation (to 3σ) was observed for the Pt–N and Pt–Cl bond lengths for both compounds, nor the Pt–N–C bond angle in MgNH₂Me, throughout their respective pressure series (Tables S3 and S4, ESI†). Furthermore, no significant change was observed in the intra-chain dihedral angle in MgNH₃ (Table S3, ESI†). Therefore, due to the lack of structure variation, the response of MgNH₃ to the application of pressure can be interpreted simply by its unit cell compression. On the other hand, a small but significant (to 3σ) increase in the Cl–Pt··Pt–N torsional angle from 31.9(3)° to 33.4(4)° was observed in MgNH₂Me between ambient pressure and 1.92 GPa (Table S4, ESI†). It appears that modifying the [Pt(NH₂R)₄]²⁺ component has caused the structure to become more flexible in the [110] direction, which facilitates greater compression along the *a/b* axes and thus reduces the propensity for compression along the Pt··Pt stacking direction.

Between 1.61 and 1.96 GPa, the compression along the *c* axis direction in MgNH₂Me almost completely stalled, and therefore contraction of the Pt··Pt stacking distance was also negligible across this pressure range; it appears that the extra steric bulk associated with the amine ligand had caused the system to lock

and reach an impasse in terms of *c* axis contraction. The diffraction data collected at the final pressure point of 2.34 GPa could not be indexed in the *P4/mnc* space group, but rather in the lower symmetry *C2/c* space group (Table S2, ESI†), with a sharp decrease in the *c* axis parameter from 6.32 Å to 6.27 Å, which would correspond to a decrease in the Pt··Pt stacking distance. A phase transition has therefore taken place, potentially in order to allow further compression along the *c*-axis direction. Although we have been unable to solve the post-phase transition structure, the lowering of symmetry, *via* an unobserved intermediate orthorhombic structure, to the monoclinic *C2/c* space group would cause a slanting of the stacking chains. Despite the decrease in the Pt··Pt stacking distance, such a slanting could result in a weakening of the intra-chain interactions (the nature of which will be illustrated in the next section), which could slow, or even reverse, the conductivity-pressure response. This result highlights that structural modifications must be studied carefully because, although not disrupting the ambient pressure crystal packing, they could cause unwanted phase transitions to occur at higher pressures, possibly resulting in the loss of desirable behaviour.

Solid state electronic band structure calculations of ambient pressure structures

The complete unit cell electronic band structure obtained for the ambient structure of MgNH₃ (Fig. 3) using the HSE06 hybrid-DFT functional revealed that the structure possesses an indirect (*M* → *Γ*) band gap of 1.56 eV. This is somewhat larger than those obtained from the previous calculations using the 1D MgNH₃ model (*ca.* 1 eV) which were based on pure DFT methods alongside a Fock matrix diagonalisation scheme, highlighting the differences in dealing with the electron exchange.^{30,35} Nevertheless, the shapes of the frontier bands are in agreement with those reported (between *Γ* and *X* only) for the 1-D MgNH₃ model.³⁰ The highest occupied crystalline orbital (HOCO) is highly dispersive with respect to the *k*-point

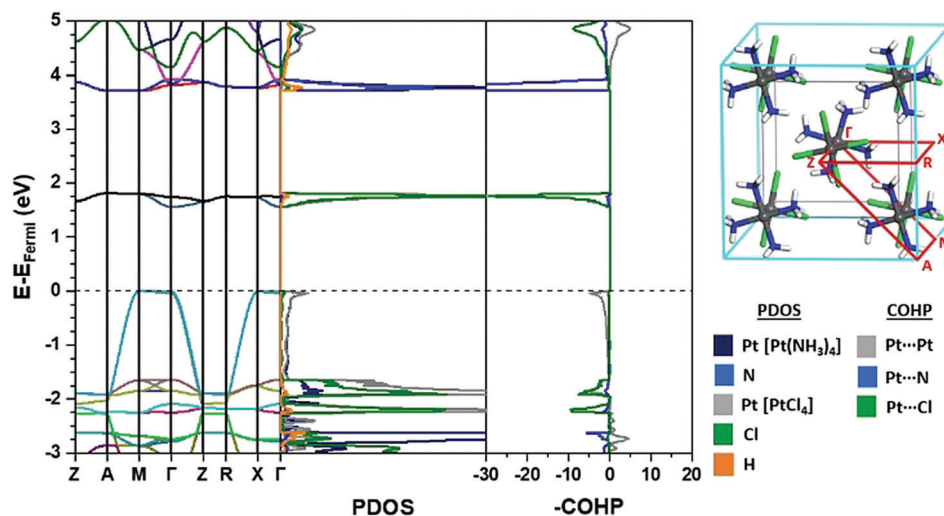


Fig. 3 Left: Electronic band structure, projected density of states (PDOS) and COHP plot of the ambient pressure structure of MgNH₃. Right: Real space (grey) and reciprocal (light blue) lattices of MgNH₃, with the Brillouin zone path used in the electronic band structure coloured in red. $E_{\text{Fermi}} = -4.853$ eV.



path $\Gamma \rightarrow Z$ (and $A \rightarrow M$, $R \rightarrow X$), corresponding to strong interactions along the directions of the $\text{Pt} \cdots \text{Pt}$ stacking. The band flattens along $M \rightarrow \Gamma$ (and $Z \rightarrow A$, $Z \rightarrow R$, $X \rightarrow \Gamma$), reflecting a lack of inter-column interactions. In contrast, the lowest unoccupied crystalline orbital (LUCO) is mostly k -invariant, which suggests a highly localised orbital unaffected by the interactions from neighbouring molecules in all directions through the unit cell.

Further information was gained from the projected density of states (PDOS), which identifies the contribution of each atom type to each band, and from the crystalline overlap Hamiltonian population (COHP) plot, which utilises the combination of the density of states and Hamiltonian population to provide a description (antibonding or bonding for negative and positive values respectively, using $-\text{COHP}$ values by convention) of interactions between specified atom types for each band, shown in Fig. 3. The HOCO for MgNH_3 mainly consists of contributions from the Pt atoms in both fragments in an antibonding configuration, whereas the contribution to the LUCO is almost exclusively from atoms in the $[\text{PtCl}_4]$ component in the form of $\text{Pt} \cdots \text{Cl}$ antibonding interactions. These orbital descriptions match that found in the previous DFT study on the 1-D model,³⁰ as well as to the calculated visualised HOCO and LUCO, generated at the Γ k -point, as shown in Fig. 4.

Examination of the band structure, PDOS, COHP plot and crystalline orbital visualisations of MgNH_2Me (Fig. 5 and 6) highlight that the ligand modification had a minimal effect on the electronic properties; the nature of the frontier bands are very similar to those observed for MgNH_3 . A slightly larger ambient pressure band gap (1.71 eV) was calculated for MgNH_2Me , resulting from a subtle difference in the weak $\text{Pt} \cdots \text{Pt}$ interactions observed in the LUCO band. In MgNH_3 , this interaction is bonding in nature, thus lowering the LUCO energy from its position if no $\text{Pt} \cdots \text{Pt}$ interaction was present, whereas in MgNH_2Me the slightly larger $\text{Cl}-\text{Pt} \cdots \text{Pt}-\text{N}$ dihedral angle resulted in this interaction being anti-bonding, raising the LUCO energy. COHP plots enlarged to show the $\text{Pt} \cdots \text{Pt}$ interaction in the LUCO more clearly are presented in the supplementary information (Fig. S4 and S5, ESI†).

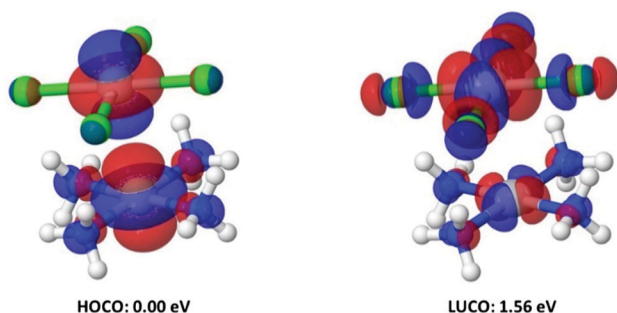


Fig. 4 Highest occupied (left) and lowest unoccupied (right) crystalline orbitals of MgNH_3 . Energies expressed at the Γ k -point, adjusted with respect to the Fermi energy surface. Atoms are coloured: Pt (grey), Cl (green), N (blue), H (white). A greater selection of the visualised orbitals near the band gap are provided in the ESI† (Fig. S2).

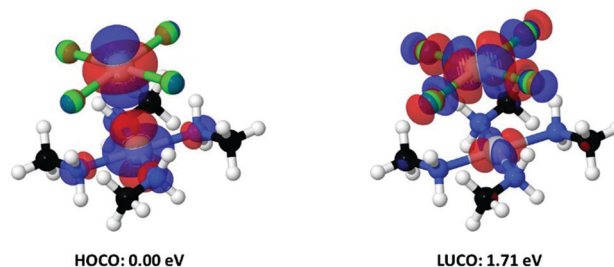


Fig. 5 Highest occupied (left) and lowest unoccupied (right) crystalline orbitals of MgNH_2Me , with their respective Fermi level adjusted energies obtained at the Γ k -point. Atoms are coloured: Pt (grey), Cl (green), N (blue), C (black), H (white). A greater selection of the visualised orbitals near the band gap are provided in the ESI† (Fig. S3).

Solid state electronic band structure calculations of high-pressure structures

By analysing the results from similar calculations on the structures of MgNH_3 and MgNH_2Me obtained experimentally under high-pressure, the response of the electronic properties to pressure could be evaluated. The electronic band structures calculated for the 4.56 GPa and 1.92 GPa structures for MgNH_3 (Fig. S6, ESI†) and MgNH_2Me (Fig. S7, ESI†) reveal very similar frontier orbitals to that observed for the ambient pressure structures, with the greatest difference attributed to an increase in dispersion in the HOCO band along $\Gamma \rightarrow Z$ (and $A \rightarrow M$, $R \rightarrow X$) indicating a strengthening of the $\text{Pt} \cdots \text{Pt}$ interaction which is the expected result of contraction along the c axis direction. This was further verified by examining the absolute energies of the HOCO and LUCO across the pressure series (Fig. S8, ESI†); the HOCO energy for both compounds was shown to increase steadily with increasing pressure, whereas the change in the LUCO energy was minimal. Therefore, the closure of the band gap in both compounds could be almost exclusively attributed to the continuous destabilisation of the HOCO. This result is in stark contrast to the change in the orbital energies observed previously for $\text{Pt}(\text{bqd})_2$, in which interlayer contraction resulted in destabilisation of the HOCO and stabilisation of the LUCO, causing the energies to converge at 1 GPa, at which point the metallic state is formed (Fig. S9, ESI†).²³

The band gap of MgNH_3 decreased to 0.82 eV by 4.62 GPa, approximately half of the band gap obtained at ambient pressure; this equates to an average compression rate of $-0.16 \text{ eV GPa}^{-1}$. If this average band gap compression rate was extrapolated to higher pressures, it is predicted that the metallic state of MgNH_3 could be observed at around 9.7 GPa. This pressure requirement to form the metallic state is in good agreement with the pressure at which the peak conductivity was observed experimentally at around 10 GPa.²⁶ However, expecting this rate of compression to be maintained up to 10 GPa is an oversimplification, given the rate of unit cell compression was observed to decrease throughout the pressure series (Fig. 2).

An alternative to analysing the band gap response with respect to pressure, Fig. 7 shows the band gap response of both Magnus salts to contraction of the $\text{Pt} \cdots \text{Pt}$ stacking



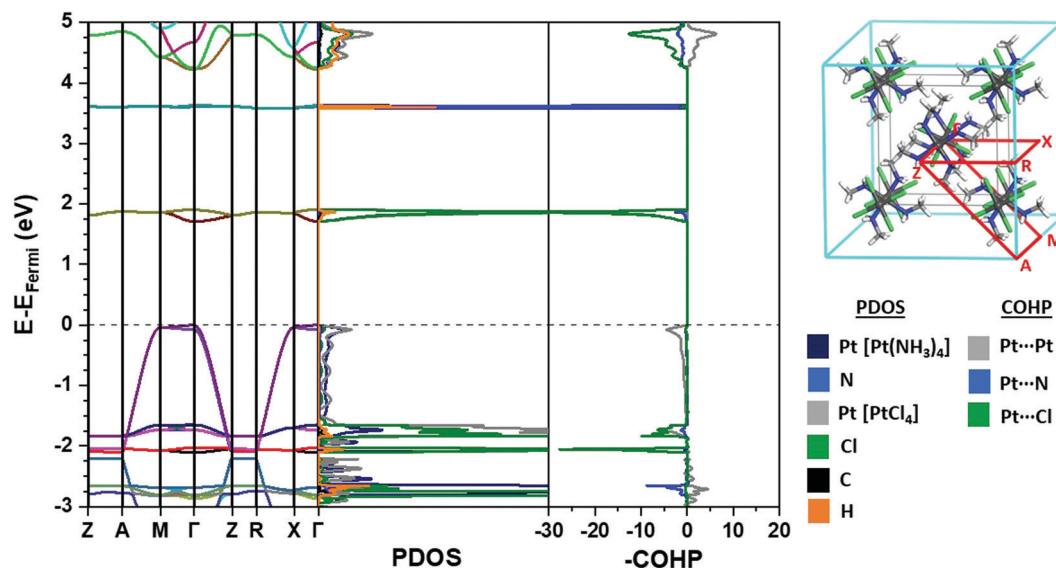


Fig. 6 Left: Electronic band structure, projected density of states and $-COHP$ plot of the ambient pressure structure of $MgNH_2Me$. Right: Real space (grey) and reciprocal (light blue) lattices of $MgNH_2Me$, with the Brillouin zone path used in the electronic band structure coloured in red. $E_{Fermi} = -4.656$ eV.

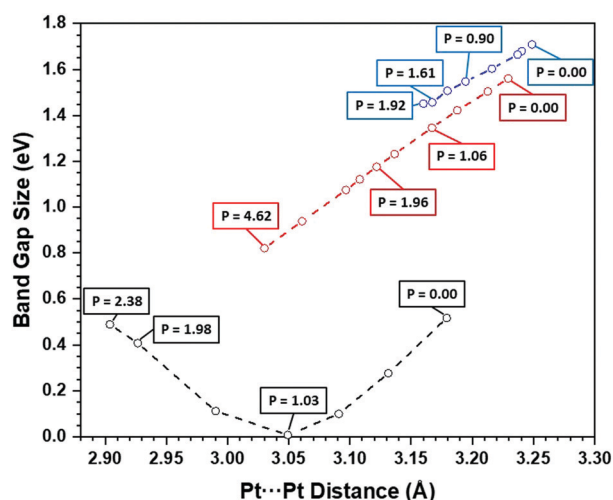


Fig. 7 Band gap energy of $MgNH_3$ (red) and $MgNH_2Me$ (blue) plotted against intra-column $Pt \cdots Pt$ distance, alongside $Pt(bqd)_2$ (black) for ref. 23. Shorter $Pt \cdots Pt$ distances signify higher pressures as a result of unit cell contraction. The associated pressures of certain points are provided as in-graph captions; pressure units are GPa.

distance, in comparison to those values previously determined for $Pt(bqd)_2$.²³ This figure clearly shows the stark difference in band gap behaviour between $Pt(bqd)_2$ and the two Magnus salt complexes. The rate of compression for $MgNH_3$ is linear throughout the pressure series, equalling -3.72 eV \AA^{-1} ; if this rate were extrapolated out further, it is predicted the $MgNH_3$ band gap would close by a $Pt \cdots Pt$ distance of 2.80 \AA . A solid state calculation on an optimised structure of $MgNH_3$ with an artificially compressed c axis ($Pt \cdots Pt$ distance = 2.76 \AA , Fig. 8), revealed that the metallic state is indeed formed upon this extent of $Pt \cdots Pt$ contraction, indicated by the overlap of the

HOCO and LUCO bands in the electronic band structure. Previous experimental studies showed that this extent of $Pt \cdots Pt$ contraction is not observed below 13 GPa,³⁶ whereas the maximum conductivity was observed at 10 GPa prior to a decrease in conductivity;²⁶ there is an apparent mismatch between the multiple studies, including our own, for when, or if, the metallic state in $MgNH_3$ is exhibited.

The band gap of $MgNH_2Me$ at 1.61 GPa was calculated as 1.46 eV (Fig. S8, ESI†), hence resulting in an average compression rate of -0.16 eV GPa^{-1} , a slightly slower compression rate than that seen for $MgNH_3$ over a similar pressure range, due to the lesser extent of contraction along the $Pt \cdots Pt$ stacking direction. The rate of band gap compression with respect to contraction of the $Pt \cdots Pt$ distance was also slightly lower (-3.08 eV \AA^{-1}) than that seen for $MgNH_3$ (Fig. 7); this is likely caused by the slight destabilisation of the $MgNH_2Me$ LUCO across the pressure series (Fig. S8, ESI†) due to the strengthening of the weak $Pt \cdots Pt$ antibonding interaction in the LUCO band (Fig. S5, ESI†) resulting in a minor suppression of the band gap closure, with the opposing behaviour observed in $MgNH_3$ (Fig. S4, ESI†). By 1.92 GPa, the band gap compression in $MgNH_2Me$ had plateaued (Fig. 7), hence resulting in a band gap of 1.45 eV (Fig. S8, ESI†) prior to the structural phase transition. Overall, the similar results obtained for $MgNH_2Me$ compared to $MgNH_3$ are perhaps not surprising, given the previous DFT study on $MgNH_3$ predicted that an alkyl substitution of the ammonia ligand would not alter the nature of the frontier bands.³⁰ The slower band gap response to pressure, which had previously not been considered, is attributed to subtle differences in the structural response and intermolecular interactions.

Comparing the results of the solid state calculations for $MgNH_3$ to those from the previous study on $Pt(bqd)_2$ reveal the



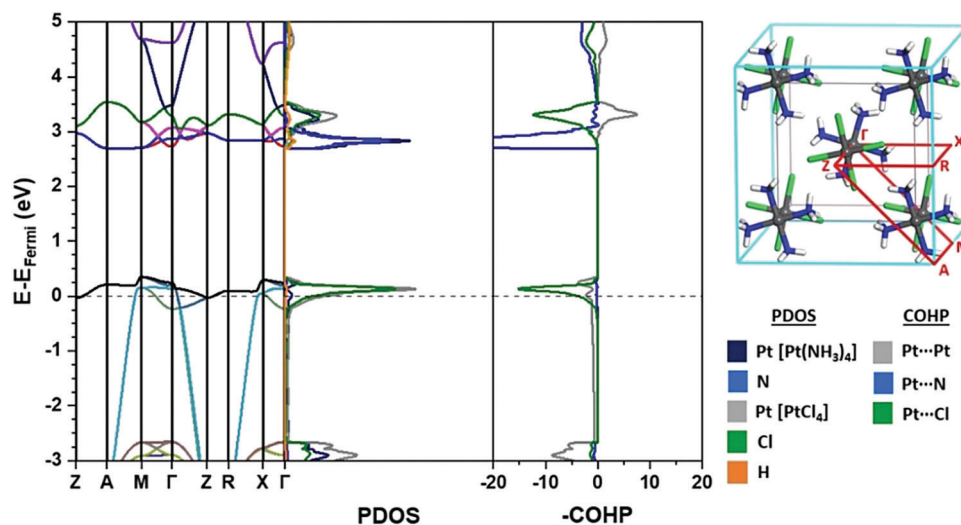


Fig. 8 Electronic band structure, projected density of states (PDOS) and $-COHP$ plot of the theoretical structure of $MgNH_3$ where $a = 8.77$ Å, $c = 5.52$ Å. Right: Real space (grey) and reciprocal (light blue) lattices of $MgNH_2Me$, with the Brillouin zone path used in the electronic band structure coloured in red. $E_{Fermi} = -3.605$ eV.

key difference in the differing electronic behaviour of these two materials. The HOCO for both compounds are very similar, and hence contribute to the band gap compression in a similar manner throughout the pressure series. However, as previously discussed, the LUCO for $MgNH_3$ and $MgNH_2Me$ are very localised, and thus their energies have an almost negligible response to pressure, which is in stark contrast to the delocalised LUCO for $Pt(bqd)_2$. The ligand...ligand and Pt...Pt intermolecular bonding contributions to the LUCO in $Pt(bqd)_2$ cause the LUCO to stabilise throughout the pressure series (Fig. S9, ESI†), hence the rate of band gap compression in $Pt(bqd)_2$ is accelerated by the change in energy of both frontier bands until they converge to form the metallic state, and then move pass each other at even higher pressures.²³ $MgNH_3$, with its larger ambient pressure band gap and lower band gap compression rate, facilitated by solely HOCO destabilisation, requires much greater inputs of pressure to come close to forming the metallic state.

Conclusions

In this study the complementary techniques of high-pressure single crystal X-ray diffraction and electronic band structure calculations have successfully been utilised to provide a full characterisation of the structural and electronic changes that occur in $MgNH_3$ and $MgNH_2Me$ under pressure. Both compounds show similar volumetric compression, achieving around 8% compression by 2 GPa. The majority of compression in $MgNH_3$ can be attributed to the Pt...Pt stacking direction, whereas equal contribution from the a/b and c axes directions was observed for the methylamine derivative due to the larger and more flexible ligand component resulting in a less rigid packing structure. Furthermore, while no difference in the ambient-pressure crystal packing is caused by the ligand

modification, an unexpected phase transition in $MgNH_2Me$ was observed at *ca.* 2 GPa, resulting in alleviating the restricted compression along the c axis direction. Further work would be required to evaluate if this phase transition had an adverse effect on the band gap compression, but nevertheless this result highlights the complications caused by even subtle structural modifications.

The solid state calculations on both compounds produced full electronic band structures for the first time; the results for the intra-column component are in good agreement with those obtained from previous one-dimensional studies,³⁰ with larger band gap values observed in this study due to the use of hybrid-DFT functionals. The description of the HOCO and LUCO for both compounds, anti-bonding $Pt(d_{z^2}) \cdots Pt(d_{z^2})$ and $Pt(d_{x^2-y^2}) \cdots Cl(p_{x/y})$ respectively, matched those described previously in the literature,³⁰ and highlight that the frontier orbitals are not altered by the ligand modification. It was also revealed from calculations that the metallic state of $MgNH_3$ is achieved upon Pt...Pt contraction to below 2.80 Å; further experimental work will be required to confirm this result and ascertain the pressure inputs required; results from previous studies suggest this will not be achieved until 10–15 GPa.²⁶

An examination of the absolute HOCO and LUCO energies has shown that the band gap compression in $MgNH_3$ and $MgNH_2Me$ can be described almost exclusively from an energy change of the former, caused by Pt...Pt compression, while the highly localised nature of the latter causes it to respond almost negligibly to pressure. This differs greatly from the results previously observed for $Pt(bqd)_2$, in which the more delocalised LUCO plays a more active role to band gap compression.²³ Hence, across these two all-encompassing studies, a much greater understanding has been gained on how two compounds with very similar starting Pt...Pt distances can possess very different electronic properties. The correct crystal packing and short metal...metal distances are not the sole identifiers of a



highly-responsive piezoresistive material; a further requirement is for delocalised frontier orbitals, both of which possessing strong contributions from intermolecular interactions. This combination facilitates both smaller ambient pressure band gaps and faster band gap compression, and thus smaller pressure inputs are required to obtain the desired metallic state.

Methods

Sample preparation

[Pt(NH₃)₄][PtCl₄]. A solution of Pt(NH₃)₄·2Cl (50 mg, 0.15 mmol) in water (2 ml) was layered cautiously on top of a solution of K₂PtCl₄ (62 mg, 0.15 mmol) in water (2 ml). The mixture was left to stand, and green crystals formed over time, which were collected *via* filtration (72 mg, 64%).

[Pt(NH₂CH₃)₄][PtCl₄]. A solution of Pt(NH₂CH₃)₄·2Cl (50 mg, 0.12 mmol) in water (2 ml) was layered cautiously on top of a solution of K₂PtCl₄ (53 mg, 0.13 mmol) in water (2 ml). The mixture was left to stand, and green-blue crystals formed over time, which were collected *via* filtration (74 mg, 72%).

Ambient pressure X-ray diffraction data collection

Data were measured using ω scans using Cu-K α X-ray radiation on an Oxford Diffraction SUPERNOVA diffractometer. The diffraction pattern was indexed and the total number of runs and images based on the strategy calculation from the program CrysAlisPro.³⁷ Data reduction, scaling and absorption corrections were performed using CrysAlisPro.³⁷ The structure was solved and the space group determined by the Sir92 structure solution program using direct methods and refined by full matrix least squares minimisation on F^2 using CRYSTALS.^{38,39} All non-hydrogen atoms were refined anisotropically. Hydrogen atom positions were calculated geometrically for the model for MagNH₂Me. For MagNH₃, hydrogen atoms were found in a difference map and then refined using constraints (to maintain the tetrahedral geometry of the NH₃ group).

High pressure X-ray diffraction data collection

High-pressure diffraction experiments were undertaken on a single crystal of MagNH₃, loaded in a modified Merrill-Bassett diamond anvil cell alongside a ruby crystal (acting as the in-situ pressure calibrant) and the hydrostatic pressure transmitting medium Fluorinert FC-70 (perfluorotri-*N*-pentylamine).⁴⁰ The diffraction data for all non-ambient pressure points were obtained at the Diamond Light Source i19-EH2 beamline,⁴¹ utilising the Pilatus 300K detector and tuneable monochromatic X-ray radiation set to 0.4859 Å (25.5 keV). Data reduction, scaling and absorption corrections were performed using CrysAlisPro.³⁷ In order to obtain the MagNH₃ structure solution at each pressure point, the ambient pressure structure was allowed to refine in CRYSTALS against each set of integrated high pressure data.³⁹ The refinement was carried out against F^2 in all cases. All 1,2 and 1,3 distances were restrained according to values observed in the ambient pressure structure. The same process of data collection, integration, structure solution and

refinement was utilised for MagNH₂Me. For all the high-pressure structures obtained in this study, the non-hydrogen atoms were refined anisotropically with thermal and vibrational similarity restraints applied across the ligands. For MagNH₂Me, all hydrogen atoms were placed geometrically and the positions were allowed to ride during the refinement process. For MagNH₃, hydrogen atoms were located in a difference map, and refined with constraints as in the ambient pressure structure.

Computational methodology

All solid state calculations have been performed using CRYSTAL17,^{42,43} where DFT or hybrid-DFT functionals are implemented with crystalline orbitals built from linear combinations of atomic orbitals. Developed from Gaussian-type functions for solid state periodic systems, a triple zeta valence with polarization quality basis set was utilised for Cl atoms,⁴⁴ 6-311G(d) basis sets were utilised for N and C atoms,⁴⁵ and a 3-1(p)1G basis set was utilised for H atoms.⁴⁶ For Pt the scalar-relativistic pseudopotential as developed by Andrae *et al.* was employed to treat 60 core electrons;⁴⁷ the remaining [4s4p2d] valence electrons were treated explicitly, as described in the methodology by Doll.⁴⁸ X-ray crystal structures determined in this work were used as input geometries for the optimisations.

Multiple functionals were utilised for an initial set of optimisation calculations on the ambient pressure MagNH₃ starting model in order to determine the most suitable functional for this study; both pure DFT (PBE, BLYP) and already-constructed hybrid DFT (B3LYP, HSE06, PBE0) functionals were tested, with the latter being used to avoid the complication of utilising a separate Fock-matrix diagonalisation scheme as observed in the previous computational study on MagNH₃.³⁰ Taking into account the experimental and calculated Pt–N and Pt–Cl bond lengths and unit cell parameters (Table S5, ESI[†]), it was determined that HSE06 was the most suitable choice of functional. Our choice was further justified by literature examples of its excellent performance in calculating band gaps compared to its GGA and global screen counterparts,^{45,49,50} even for complexes containing heavy elements for which spin-orbit coupling normally plays a prominent role on the electronic behaviour of the material.^{51,52}

Moreover, in our previous study investigating the solid state electronic properties of Pt(bqd)₂,²³ HSE06 performed better than other hybrid-DFT functionals in calculating the electronic properties of Pt(bqd)₂ throughout its pressure series, which were in strong agreement with literature band-gap values and providing a valid explanation for the electronic transitions observed experimentally. However, the agreement between the experimental and calculated unit cell parameters of MagNH₃ was not sufficient, with the D3 dispersion correction causing an over-contraction of 3.9% of the inter-planar separation associated with the *c*-axis parameter (Table S6, ESI[†]). For this reason, all structural optimisations reported herein have unit cell parameters fixed at experimental values.

Structural optimisations have been performed with a Monkhorst–Pack net of 8 × 8 × 8,⁵³ corresponding to 75 *k*-points in the Brillouin zone (BZ), such that the total energy difference



obtained by using larger Monkhorst–Pack nets was smaller than 10^{-7} Hartree. From the output of these optimisation calculations, the electronic properties of the structures have been computed. Band structures, projected densities of states (PDOS), crystalline orbital plots and crystal orbital Hamiltonian population (COHP) diagrams have been produced,⁵⁴ in order to analyse the electronic composition, visualise specific crystalline orbitals and describe the nature of specified interactions of the MgNH_3 and MgNH_2Me structures obtained experimentally at various points throughout the pressure series. Calculations to generate the PDOS and COHP were run using the atomistically optimised structures as the input alongside a wavefunction from SCF cycles converged at a higher shrink level (utilising a Monkhorst–Pack net of $24 \times 24 \times 24 \times 24$,⁵³ corresponding to 1183 k -points). COHP values are determined by multiplying the density of states by the Hamilton population; the –COHP plots are presented, by convention, with the positive and negative values indicating bonding and anti-bonding interactions respectively.⁵⁵ All other optimization criteria were used as default for CRYSTAL17 (default total energy convergence threshold during optimisation (TOLDEE) of 10^{-7} Hartree, tolerance of the RMS of the gradient (TOLDEG) if 3×10^{-4} Hartree and tolerance of the RMS of the atomic displacements (TOLDEE) of 1.2×10^{-3} Hartree).

Conflicts of interest

There are no conflicts to declare.

Acknowledgements

The authors thank the Leverhulme Trust (RPG-2016-152) for funding. This work has made use of the resources provided by the Edinburgh Compute and Data Facility (ECDF) (<http://www.ecdf.ed.ac.uk/>). This work used the ARCHER UK National Supercomputing Service (<http://www.archer.ac.uk>). We acknowledge Diamond Light Source for time on Beamline I19 under Proposal MT19178 and for their assistance during the beamtime. J. R. thanks the University of Edinburgh for PhD stipend funding in the form of a Principal's Career Development Scholarship. The authors gratefully acknowledge the facilities, and the scientific and technical assistance of Microscopy Australian at the Centre for Microscopy, Characterisation & Analysis, The University of Western Australia, a facility funded by the University, State and Commonwealth Governments. We are grateful for computational support from the UK Materials and Molecular Modelling Hub, which is partially funded by EPSRC (EP/P020194), for which access was obtained *via* the UKCP consortium and funded by EPSRC grant ref EP/P022561/1.

References

- H. Akamatsu, H. Inokuchi and Y. Matsunaga, *Nature*, 1954, **173**, 168–169.
- D. Jerome, A. Mazaud, M. Ribault and K. Bechgaard, *J. Phys. Lett.*, 1980, **41**, L95–L98.
- R. Kato, H. Cui, T. Tsumuraya, T. Miyazaki and Y. Suzumura, *J. Am. Chem. Soc.*, 2017, **139**, 1770–1773.
- J. B. Torrance, J. J. Mayerle, K. Bechgaard, B. D. Silverman and Y. Tomkiewicz, *Phys. Rev. B: Condens. Matter Mater. Phys.*, 1980, **22**, 4960–4965.
- A. Kobayashi, E. Fujiwara and H. Kobayashi, *Chem. Rev.*, 2004, **104**, 5243–5264.
- Y. Le Gal, T. Roisnel, P. Auban-Senzier, N. Bellec, J. Iniguez, E. Canadell and D. Lorcy, *J. Am. Chem. Soc.*, 2018, **140**, 6998–7004.
- M. Sasa, E. Fujiwara, A. Kobayashi, S. Ishibashi, K. Terakura, Y. Okano, H. Fujiwara and H. Kobayashi, *J. Mater. Chem.*, 2005, **15**, 155–163.
- B. Zhou, H. Yajima, Y. Idobata, A. Kobayashi, T. Kobayashi, E. Nishibori, H. Sawa and H. Kobayashi, *Chem. Lett.*, 2012, **41**, 154–156.
- D. G. Branzea, F. Pop, P. Auban-Senzier, R. Clerac, P. Alemany, E. Canadell and N. Avarvari, *J. Am. Chem. Soc.*, 2016, **138**, 6838–6851.
- N. C. Schiødt, T. Bjørnholm, K. Bechgaard, J. J. Neumeier, C. Allgeier, C. S. Jacobsen and N. Thorup, *Phys. Rev. B: Condens. Matter Mater. Phys.*, 1996, **53**, 1773–1778.
- D. Belo, H. Alves, E. B. Lopes, M. T. Duarte, V. Gama, R. T. Henriques, M. Almeida, A. Perez-Benitez, C. Rovira and J. Veciana, *Chem. – Eur. J.*, 2001, **7**, 511–519.
- O. J. Dautel, M. Fourmigue, E. Canadell and P. Auban-Senzier, *Adv. Funct. Mater.*, 2002, **12**, 693–698.
- H. Tanaka, Y. Okano, H. Kobayashi, W. Suzuki and A. Kobayashi, *Science*, 2001, **291**, 285–287.
- B. Zhou, S. Ogura, Q. Z. Liu, H. Kasai, E. Nishibori and A. Kobayashi, *Chem. Lett.*, 2016, **45**, 303–305.
- N. Tenn, N. Bellec, O. Jeannin, L. Piekara-Sady, P. Auban-Senzier, J. Iniguez, E. Canadell and D. Lorcy, *J. Am. Chem. Soc.*, 2009, **131**, 16961–16967.
- H. B. Cui, T. Tsumuraya, T. Miyazaki, Y. Okano and R. Kato, *Eur. J. Inorg. Chem.*, 2014, 3837–3840.
- J. W. Brill, M. Megnamisibombe and M. Novotny, *J. Chem. Phys.*, 1978, **68**, 585–592.
- K. Takeda, I. Shirotani, C. Sekine and K. Yakushi, *J. Phys.: Condens. Matter*, 2000, **12**, L483–L488.
- K. Takeda, I. Shirotani and K. Yakushi, *Chem. Mater.*, 2000, **12**, 912–916.
- K. Takeda, I. Shirotani and K. Yakushi, *Synth. Met.*, 2003, **133**, 415–416.
- I. Shirotani, J. Hayashi and K. Takeda, *Mol. Cryst. Liq. Cryst.*, 2005, **442**, 157–166.
- K. Takeda, I. Shirotani, J. Hayashi, H. Fukuda and K. Ito, *Mol. Cryst. Liq. Cryst.*, 2006, **452**, 113–122.
- H. Benjamin, J. G. Richardson, S. A. Moggach, S. Afanasjevs, L. Warren, M. R. Warren, D. R. Allan, C. A. Morrison, K. V. Kamenev and N. Robertson, *Phys. Chem. Chem. Phys.*, 2020, **22**, 6677–6689.
- M. Megnamisibombe, *J. Solid State Chem.*, 1979, **27**, 389–396.
- E. Frasson, C. Panattoni and R. Zannetti, *Acta Crystallogr.*, 1959, **12**, 1027–1031.



- 26 L. V. Interrante and F. P. Bundy, *Inorg. Chem.*, 1971, **10**, 1169.
- 27 M. Atoji, J. W. Richardson and R. E. Rundle, *J. Am. Chem. Soc.*, 1957, **79**, 3017–3020.
- 28 C. M. Edwards and I. S. Butler, *Inorg. Chim. Acta*, 2011, **377**, 155–158.
- 29 M. E. Cradwick, D. Hall and R. K. Phillips, *Acta Crystallogr., Sect. B: Struct. Crystallogr. Cryst. Chem.*, 1971, **27**, 480.
- 30 E. G. Kim, K. Schmidt, W. R. Caseri, T. Kreouzis, N. Stingelin-Stutzmann and J. L. Bredas, *Adv. Mater.*, 2006, **18**, 2039–2043.
- 31 M. Megnamisibelombe, *J. Solid State Chem.*, 1977, **22**, 151–156.
- 32 I. Shirotani, A. Kawamura, K. Suzuki, W. Utsumi and T. Yagi, *Bull. Chem. Soc. Jpn.*, 1991, **64**, 1607–1612.
- 33 T. Varga, A. P. Wilkinson and R. J. Angel, *Rev. Sci. Instrum.*, 2003, **74**, 4564–4566.
- 34 F. Birch, *Phys. Rev.*, 1947, **71**, 809–824.
- 35 W. T. Pollard and R. A. Friesner, *J. Chem. Phys.*, 1993, **99**, 6742–6750.
- 36 L. V. Interrante and F. P. Bundy, *J. Chem. Soc. D*, 1970, 584–586.
- 37 CrysAlisPRO, Oxford Diffraction/Aligent Technologies UK Ltd., Yarnton, UK.
- 38 A. Altomare, G. Cascarano, G. Giacovazzo, A. Guagliardi, M. C. Burla, G. Polidori and M. Camalli, *J. Appl. Crystallogr.*, 1994, **27**, 435.
- 39 P. W. Betteridge, J. R. Carruthers, R. I. Cooper, K. Prout and D. J. Watkin, *J. Appl. Crystallogr.*, 2003, **36**, 1487.
- 40 S. A. Moggach, D. R. Allan, S. Parsons and J. E. Warren, *J. Appl. Crystallogr.*, 2008, **41**, 249–251.
- 41 H. Nowell, S. A. Barnett, K. E. Christensen, S. J. Teat and D. R. Allan, *J. Synchrotron Radiat.*, 2012, **19**, 435–441.
- 42 R. Dovesi, R. Orlando, B. Civalleri, C. Roetti, V. R. Saunders and C. M. Zicovich-Wilson, *Z. Kristallogr.*, 2005, **220**, 571–573.
- 43 R. Dovesi, A. Erba, R. Orlando, C. M. Zicovich-Wilson, B. Civalleri, L. Maschio, M. Rerat, S. Casassa, J. Baima, S. Salustro and B. Kirtman, *Wiley Interdiscip. Rev.: Comput. Mol. Sci.*, 2018, **8**, e1360.
- 44 M. F. Peintinger, D. V. Oliveira and T. Bredow, *J. Comput. Chem.*, 2013, **34**, 451–459.
- 45 J. Heyd, J. E. Peralta, G. E. Scuseria and R. L. Martin, *J. Chem. Phys.*, 2005, **123**, 174101.
- 46 C. Gatti, V. R. Saunders and C. Roetti, *J. Chem. Phys.*, 1994, **101**, 10686–10696.
- 47 D. Andrae, U. Haussermann, M. Dolg, H. Stoll and H. Preuss, *Theor. Chim. Acta*, 1991, **78**, 247–266.
- 48 K. Doll, *Surf. Sci.*, 2004, **573**, 464–473.
- 49 A. V. Krukau, O. A. Vydrov, A. F. Izmaylov and G. E. Scuseria, *J. Chem. Phys.*, 2006, **125**, 224106.
- 50 A. J. Garza and G. E. Scuseria, *J. Phys. Chem. Lett.*, 2016, **7**, 4165–4170.
- 51 J. E. Peralta, J. Heyd, G. E. Scuseria and R. L. Martin, *Phys. Rev. B: Condens. Matter Mater. Phys.*, 2006, **74**, 073101.
- 52 X. D. Wen, R. L. Martin, L. E. Roy, G. E. Scuseria, S. P. Rudin, E. R. Batista, T. M. McCleskey, B. L. Scott, E. Bauer, J. J. Joyce and T. Durakiewicz, *J. Chem. Phys.*, 2012, **137**, 154707.
- 53 H. J. Monkhorst and J. D. Pack, *Phys. Rev. B: Solid State*, 1976, **13**, 5188–5192.
- 54 M. T. Ruggiero, A. Erba, R. Orlando and T. M. Korter, *Phys. Chem. Chem. Phys.*, 2015, **17**, 31023–31029.
- 55 T. Hughbanks and R. Hoffmann, *J. Am. Chem. Soc.*, 1983, **105**, 3528–3537.

